Fuel 324 (2022) 124070

Contents lists available at ScienceDirect

Fuel

journal homepage: www.elsevier.com/locate/fuel

Full Length Article

A comparative evaluation of waste wood and herbaceous biomass fireside corrosion behaviours

T. Sanusi, J. Sumner *, N.J. Simms

Cranfield University, School of Water, Energy & Environment, College Road, Bedfordshire MK43 0AL, United Kingdom

ARTICLE INFO

Keywords:
Fireside corrosion
Biomass and waste combustion
Condensation rate
Thermodynamics
Cation mechanisms

ABSTRACT

Biomass/biomass waste (BBW) is a renewable energy source fired in combustion power plants. However, challenges associated include accelerated 'fireside' corrosion of heat exchangers. Fireside corrosion is fuel dependent, e.g. virgin wood fuels have lower fireside corrosion risks; as such their demand and cost is high. Waste wood fuels (WWF) and herbaceous grass biomass (HGB), generate different combustion environments, influencing heat exchanger fireside corrosion damage.

This paper compares the fireside corrosion of WWF and HGB fuels to improve understanding of their attack mechanisms on T91 and 374HFG. The species generated in combustion have been investigated by thermodynamic modelling. Corrosion damage has been evaluated by high temperature corrosion furnace tests at 600 °C, employing the well-established deposit recoat method based on these evolved species. Vapour condensation fluxes have been compared for both fuel categories; corrosion rates increase with this condensation flux. Deposition fluxes from HGB fuels are higher than for WWF. For example, the average KCl deposition fluxes calculated are 1566 μg/cm^{2}h and 295 μg/cm^{2}h per kg fuel feed respectively, explaining the comparatively greater fireside corrosion rates experienced in power plants combusting HGB fuels. The deposit chemistries generated are also different: K-containing compounds only (for HGB fuels) versus K-, Na- and Ca-containing compounds (for WWF).

Evaluation of corroded samples exposed to the different deposit chemistries show increased corrosion attack to both steels under simulated WWF firing conditions than for the HGB at matched deposit flux (100 μg/cm^{2}h).

1. Introduction

The increasing utilization of biomass combustion for renewable energy generation in the UK has led to the sourcing of large quantities of woods from North America [1]. As there are associated transportation emissions and the potential impacts on land use, wood imports may not constitute a sustainable source of renewable energy [1]. Biomass combustion operations thus require a wider range of fuel options [2].

Two fuel groups of interest for this work are waste woods fuels (WWF) and herbaceous grass and biomasses (HGB). WWF are an alternative biomass which allows local sourcing (e.g. from demolition and construction activities) [3]. HGB fuels are mainly energy crops such as miscanthus [4–6]. Wood is generally characterised as having lower levels of K, Cl, Si, S, Na and Ca than other biomass/biomass waste (BBW) fuels, while HGB are characteristically high in K, Cl and Si [7,8]. The abundance of these elements influence the chemistry of phases released in combustion, which affects fireside corrosion, in particular, for components such as power plant heat exchangers [3]. Other elements, which may be associated with WWF, include Zn and Cr in trace quantities (<500 ppm) [9,10]. Though their fireside corrosion influence require investigation, the alkali metal concentrations of these fuels are considerably higher and pose greater fireside corrosion risks.

Heat exchangers, which are usually manufactured from steel, become coated in the deposits generated from fuel combustion. By evaluating the different combustion chemistries, the nature of heat exchanger deposits can be determined. In particular, when studying heat exchanger alloys' fireside corrosion responses, the evaluation of species that are liquid at their typical surface temperatures (in biomass combustion plants ≈450-600℃ [11]), is necessary [12]. These relatively low melting point species (whose melting point can be lower than heat exchanger temperatures upon interaction with steel components [12]) make up the condensate fraction of the heat exchanger deposits and have been studied previously. For example, the corrosivity of K, Na and Ca chlorides on austenitic steel, 304L, was investigated at 600 °C by

* Corresponding author.
E-mail address: j.sumner@cranfield.ac.uk (J. Sumner).

https://doi.org/10.1016/j.fuel.2022.124070
Received 5 May 2021; Received in revised form 4 February 2022; Accepted 30 March 2022
Available online 13 May 2022
0016-2361/© 2022 The Authors. Published by Elsevier Ltd. This is an open access article under the CC BY-NC-ND license (http://creativecommons.org/licenses/by-nc-nd/4.0/).

Karlsson et al. [13]. In contrast to Na and K chloride salts, $CaCl_2$ resulted in significantly less corrosion damage (higher melting point than Na and K salts). Research comparing K_2CrO_4 formation on Fe18Cr10Ni stainless steels exposed to KCl, K_2CO_3 and K_2SO_4 at 600 °C in a 5%–O_2, 40%–H_2O (bal. N_2) atmosphere could only confirm the presence of the chromate on the samples exposed with the chloride and carbonate salts (lower melting points than the sulphate) [6].

The absolute content of elements in a fuel isn't the only determinant of their impact on fireside corrosion; the release fraction of these species is also important, as are the interactions between species after they are released. The Si content, relative to the K content of a fuel (Si/K mole ratio), is important for estimating the fraction of K that forms silicates during combustion. As K-containing silicates tend to be inert at heat exchanger temperatures, higher Si/K ratios reduce the fraction of K which remains available to form the lower melting point salts needed for fireside corrosion [14]. When studying biomass responses during combustion, the combustion compounds formed from HGB fuels may contain significant K-Si interactions [15,16]. K-Si interactions (and those of other high temperature K compounds occurring for WWF combustion) however, require further investigation.

The need to compare corrosive properties of fuel groups rather than individual fuels, arises where a wide range of elemental variations exists within each category [3,9]. Fuel category corrosion descriptions are beneficial for mixed BBW combustion streams, especially for alternative fuels where mixed combustion (for meeting fuel supply needs) is more applicable [3]. Reported differences between the average corrosion rates for WWF and HGB fuels [3] may not be solely determined by condensable compound fluxes on heat exchanger surfaces. Indeed, it is necessary to evaluate the corrosion significance of the fuels' condensing compounds' compositions. In this paper, the impacts of these biomass categories on fireside corrosion are compared.

2. Methodology

First, thermodynamically predicted species formed post-combustion for both fuel categories were calculated. Then these species were used to generate deposits for fireside corrosion tests on two conventional heat exchanger steels, using the deposit recoat method [17–20]. Corrosion assessment has been carried out by dimensional metrology [21,22], scanning electron microscopy and energy dispersive X-ray spectroscopy (SEM-EDX). Finally, calculations has been used to compare both fuel categories' vapour condensation rates.

2.1. Fuel analysis

Table 1 summarises the fuel details for 23 fuels within the WWF category and 31 within the HGB one, including the median concentration values of the ultimate analysis elements (C, H, N, O, S & Cl) for both. Individual fuel analysis reports were sourced from an online biomass and waste database, ECN Phyllis 2 [23]. presents the minor element concentrations (median values) for both fuel categories.

2.2. Thermodynamic equilibrium simulation

The ultimate analyses' (C, O, H, N, S, Cl) and minor elements' (Si, P, Fe, K, Na, Ca, Mg & Al) median concentration values for the selected WWF and HGB fuels have been used as input data to thermodynamic simulations, enabling the generation of post-combustion compounds (under the assumption of equilibrium). The use of median, instead of mean, values reduced errors by limiting the effect of extreme concentrations values included within the selected fuel categories. The use of extreme values (for specific fuel types) could be investigated in future research. Thermodynamic combustion simulations were carried out using MTData (Multiphase Thermodynamic) software [24], which applies Gibbs free energy minimisation principles. A series of multi-component phase equilibrium calculations enabled prediction of WWF and HGB combustion products within the temperature range 300-1300℃ at 1 atm. These calculations used 4:1 (HGB) and 8:1 (WWF) air/fuel mass feed ratios; adjusted to give O_2 levels of 7–8 mol.% (to simulate biomass firing flue gas conditions).

Table 1
Types of fuels listed in each fuel category, ultimate and proximate analysis, and heating values based on fuel category median elemental values. Individual fuel data have been sourced from ECN Phyllis database for biomass and waste [23].

	HGB		WWF
Fuel types	Switchgrass	Brassica	Demolition wood
	Reed canary	Courgette plant	Particle board
	Cane	Cucumber plant	Treated wood
	Barley straw	Melon plant	Painted wood
	Wheat straw	Pepper plant	Railway ties
	Sweet sorghum	Tomato plant	
	Kenaf	Watermelon	
	Rapeseed straw	Thistle	
	Miscanthus	Tobacco	
	Flax	Threshed hay	
	Aubergine plant	Grass pellets	
	Bean plant	Brassica	
Total		*31 fuels*	*23 fuels*
Analysis (wt.%)	C: a.r.* (dry)	15.94 (45.80)	40.77 (49.65)
	O: a.r.* (dry)	14.93 (40.45)	34.00 (40.01)
	H: a.r.* (dry)	2.12 (5.80)	4.88 (5.75)
	N: a.r.* (dry)	0.58 (1.08)	0.61 (0.69)
	S: a.r.* (dry)	0.05 (0.14)	0.05 (0.06)
	Cl: a.r.* (dry)	0.18 (0.22)	0.07 (0.08)
	Volatile matter (dry)	76.40 (median), 75.76 (mean)	76.40 (median), 75.04 (mean)
	Fixed Carbon (dry)	16.50	19.13
	Ash (dry)	7.91	2.70
	Moisture ([1]a.r.)	65.2	12.9
	LHV** (MJ/kg)	4	14
	HHV*** (MJ/kg)	6	15

* As received.
** Low heating value.
*** High heating value.

2.3. Deposits and test gas formulations

MTData predictions resulted in the formation of over a thousand thermodynamically stable species for each biomass fuel category; as such corrosion test deposits and gas compositions were derived from simplified thermodynamic output data, where concentrations below 10^{-5} mol/kg were eliminated. The non-gaseous species present at 600 °C are presented in Table 3. The synthetic deposit compositions were molar ratios of the condensates predicted to be present between 450 and 600℃ (i.e., expected metal surface temperatures [11]) and whose gaseous forms exist at 600-1100℃ (i.e., likely combustion gas temperatures [11]). These condensed compounds are, from here on, referred to as the key condensed phases (KCP).

Fig. 1 presents the temperature effect on KCP concentrations, while Fig. 2 gives the K fractions (mole % of fuel components containing K) in the gas phase for both fuel categories. Both figures were derived from the thermodynamic simulations of combustion.

The deposit chemistries (KCP compounds) at 600 °C are specified in Table 4. The test gas composition was obtained using the WWF's simulated O_2, CO_2, H_2O, SO_2 and HCl molar outputs at 1100℃ (balanced to 100% with N_2) and are presented in Table 5. The HGB test gas formulation had ~3 times the moisture and HCl content compared to that of WWF. It is expected that higher concentrations of corrosive gas contents (such as HCl) would increase corrosion rates of the alloys [25]. To simplify the comparison of HGB and WWF deposit corrosivity, the WWF test gas formulation was maintained for the evaluation of both deposits.

Table 2
Minor element values for fuel categories based on dry feedstock analysis data (data).

	Al		Ca		Fe		K		Mg		Na		P		Si	
	(Concentration mg/kg of fuel)															
	HGB	WWF	HGB	WWF	HGB	WWF	HGB	WWF	HGB	WWF	HGB	WWF	HGB	WWF	HGB	WWF
Median	710	519	9750	3758	520	640	25,405	760	1800	509	1698	790	6010	128	12,321	3000
Mean	1318	631	16,861	4045	868	959	45,477	876	6115	525	2124	829	6200	166	65,610	4882
Minimum	151	150	4945	2200	133	340	9600	370	1061	250	700	210	3178	67	7700	1135
Maximum	3700	1369	43,000	6537	2300	3800	121,500	2000	19,800	960	4400	1613	9600	410	230,100	13,000

Source [23]

Table 3
Predicted non-gaseous phase metal associations occurring at 600℃, expressed in moles/kg of fuel.

WWF (mole/kg)		HGB (mole/kg)	
*$CaSiO_3$	0.034	*K_3PO_4	0.19
*$CaMgSiO_4$	0.02	*$CaSiO_3$	0.16
KCl	0.018	*$CaMgSi_2O_6$	0.08
Na_2SO_4	0.008	KCl	0.05
$CaSO_4$	0.007	K_2SO_4	0.02
*$CaFe_2O_4$	0.005	*Na_2SiO_3	0.02
*$Al_2Na_2SiO_{16}$	0.005	*$Al_2Na_2SiO_{16}$	0.015
*$Al_2Ca_3SiO_{12}$	0.004	*$K_2Si_2O_5$	0.005
*$Ca_3P_2O_8$	0.002	Fe_2O_3	0.005
K_2SO_4	0.00016	*$CaFe_2O_4$	0.0001

* Compounds remaining in condensed phase up to 1300℃. Compounds not denoted are the KCP compounds that exist at 600 °C.

2.4. Laboratory testing of fireside corrosion

Based on the thermodynamic simulation results, laboratory testing was carried out to determine the extent of fireside corrosion.

2.4.1. Alloy compositions

The steel samples used were sectioned T91 and TP 347HFG tubes (≈15 mm chord, 15 mm long and 5 mm thickness; UK 600 grit finish). The nominal compositions of these steels are listed in Table 6.

2.4.2. Sample preparation and deposit application

The samples were cleaned in acetone and then *iso*-propanol for 10 min each in an ultrasonic bath. Initial weights were recorded, and initial dimensions were measured, using a 1 μm resolution digital micrometre.

The deposits were mixed from salts (>98% purity) and made into thick slurries, using deionised water, to enable smearing of the deposit mix upon each sample's convex face. The sample was then dried on a hot plate. Weight measurements were used to check that the desired (dry) deposit flux (±10 wt%) was achieved. The dried weight of the applied deposit was targeted at the weight equivalent of the required deposition flux.

2.4.3. Exposure conditions

Corrosion tests were performed in a vertical furnace, illustrated in Fig. 4. This setup contains a series of inlets and outlets for test gas, exhaust, and the moisture feed. Test samples were placed in ceramic crucibles positioned on round ceramic trays which were suspended within the alumina-lined furnace. Mass flow controllers were used to achieve the required flowrate (50 ml/min) in combination with deionised water, fed in via a peristaltic pump at 0.04 ml/min. The furnace temperature was maintained at 600℃ during exposure periods and cycled every 100 h. Between cycles, samples were recoated with deposit to simulate deposit build-up (recoat method) and their dry weight measured. Deposit residues were not removed from the sample. Deposit fluxes were applied at 100 μg/cm^2h for Dh and at 100, 50, 25 & 10 μg/cm^2h for Dw.

Post-exposure, the samples were cross-sectioned along their lengths after having being vacuum mounted in a low shrinkage resin (50% filled with ballotini glass beads to further reduce shrinkage), and then ground to a 1 μm finish using SiC grits and diamond paste all with oil lubricants. The initial micrometre (resolution, ±1 μm) dimensional measurements were compared with post-exposure dimensions which were obtained using an optical microscope with a high precision x-y stage linked to an image analyser. Metal thickness and sound metal change scatters were reordered from most to least (left to right) as illustrated in Fig. 3. This well-established method of corroded sample assessment [20,22,27] is documented in the BS ISO 26146:2012 standard [28]. SEM-EDX was used to characterise the samples after their exposure in terms of the damage morphologies and the distributions of the elements.

3. Results

3.1. Thermodynamic simulation data

The HGB fuel is Si- and P-rich (with – average values of Si, 65600 mg/kg; P, 6200 mg/kg) and is characterised by higher alkali metal contents (K, ~ 45500 mg/kg; Na, ~2100 mg/kg) relative to WWF (Si,

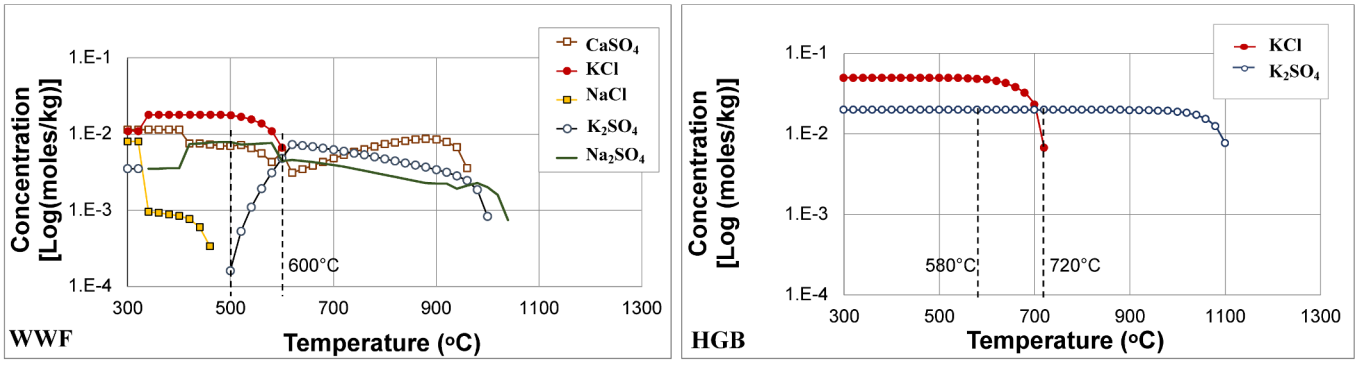


Fig. 1. MTData predicted of key condensed phases for (left) WWF and (right) HGB fuels.

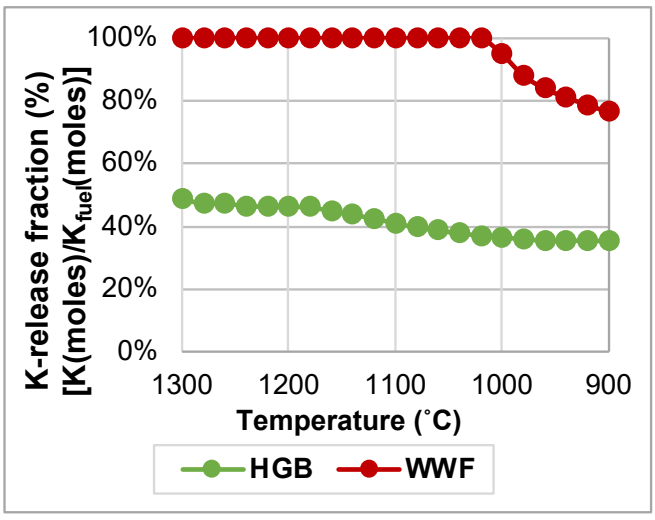


Fig. 2. Percentage of K in gas phase (mole%) for HGB and WWF.

Table 4
Deposit Dw (WWF) and Dh (HGB) compositions as molar percentages of KCP as described in Section 2.3. Values derived from thermodynamic simulations at 600 °C.

KCP*	Dw (% moles)	Dh(% moles)
KCl	30	70
K_2SO_4	20	30
Na_2SO_4	20	
$CaSO_4$	30	

* Key condensed phase compounds.

Table 5
Test gas compositions derived from thermodynamic simulation of WWF combustion gas at 1100 °C.

Components	Concentration(% moles)
H_2O	10.48
CO_2	10.03
O_2	8.47
HCl	0.0003 (3 vol ppm)
SO_2	0.0041 (41 vol ppm)
N_2 (balance)	70.96

Table 6
The nominal composition in weight percent (wt.%) of T91 and TP347HFG [18,26].

Material	C	Cr	Ni	Mo	Mn	V	Nb	Fe
TP 347HFG	0.07	18.0	10.0	–	2.0	–	1.0	Balance
T91	0.14	9	0.4	1	0.5	0.25	0.1	Balance

~4880 mg/kg; P, ~170 mg/kg; K, ~875 mg/kg, Na, ~830 mg/kg) (Table 2). From Table 3, the predominant K association formed for the HGB category at thermodynamic equilibrium is K-P (K_3PO_4; 71.6 mol.% of condensed phase K). K_3PO_4 is retained in the condensed phase beyond 1100 °C (Table 3), as such this compound is not expected condense from a vapour onto heat exchangers and so was not included as a KCP. (Note that the potential for alternative deposition mechanisms, for example inertial impaction, are not considered in this paper.) By contrast, for the WWF category, the largest K association predicted is KCl (99.1 mol.% of condensed phase K), which is classified as a KCP (transitioning from gas phase to condensed phase between the temperatures expected of the combusted gas, and the temperatures expected for the heat exchangers' surfaces). A smaller fraction of K, present as KCl (18.9 mol.% of condensed phase K), occurs within the HGB category. Na-Si associations occur for both WWF and HGB, however K-Si associations are only observed for HGB.

Within the WWF category, Ca and Na compete for Si to form higher melting point silicates (which will then not contribute to the KCP). The absence of K-P and K-Si associations or other high melting point K-compounds favour K release into the gas phase [15]. In Fig. 2, 100% K-release at 1100 °C is predicted for the WWF category. The condensation of K as low melting point salts is most feasible where other gas components, such as HCl and SO_x, are available.

The KCP temperature profiles occurring across the heat exchanger metal temperature range (≈ 450-600C), as described in Fig. 1, vary between both fuel categories. The molten fraction of Cl-phases is highest at 500–600 °C and 580–720 °C for WWF and HGB respectively (Fig. 1). The lower KCl melt range suggested for the WWF KCP system can be understood from salt equilibrium systems. Eutectic diagrams suggest the lowest melting points for K_2SO_4-KCl occurs at 713 °C (0.74/0.26 mol/mol) [30]. XRD analysis of slag in a biomass combustion furnace, reported by Niu et al. [31], verified the presence of a K_2SO_4- Na_2SO_4-KCl ternary eutectic, with the $K_3Na(SO_4)_2$ molten phase confirmed to exist at temperatures as low as 493.3 °C (712.4 K).

3.2. High temperature corrosion data

The changes in metal dimensions due to fireside corrosion following 200, 500 and 1000 h of exposure are presented in Fig. 5. The 'metal change' values at each measured point have been reordered by severity. The median metal change value for the T91-Dw samples, in increasing order of exposure times, were −112 μm, −451 μm and −659 μm, while those of T91-Dh were generally lower at −144 μm, −251 μm and −373 μm respectively. Less extensive damage was also observed on the 1000-hour exposure 347HFG-Dh sample (-191 μm metal change) than the 347HFG-Dw equivalent (-355 μm metal change).

The median internal penetration depth, which is the distance between the post-exposure median metal surface and the median sound metal penetration were within 40 μm for all samples. Scale spallation observed on the 200-hour 347HFG-Dh sample explains the usual metal loss encountered by this sample (compared to the 500-hour sample equivalent) as freshly exposed metal surface encourages accelerated corrosion attack.

The median probability metal and sound metal change values of samples exposed to Dw at varying deposit fluxes are presented in Fig. 6. The metal change ranges (highest and lowest values) for each sample are presented as error bars. The median metal change values of the Dh exposed samples at high flux (flux 100 μg/cm^{2}h) are positioned on the graphs for comparison. Metal losses on the T91 and 347HFG samples exposed to Dh at 100 μg/cm^{2}h are compared to 40 μg/cm^{2}h and 10 μg/cm^{2}h respectively for the Dw exposed samples.

At deposition fluxes of 25 μg/cm^{2}h, similar metal responses were recorded for both alloys exposed to Dw. At higher deposit fluxes (>25 μg/cm^{2}h), 347HFG offered better resistance to corrosion damage.

3.3. SEM data

Back scattered electron (BSE) images and EDX maps of the T91 and 347HFG samples were obtained. Fig. 7 gives the unexposed samples (left), and an example site from samples exposed to Dw and Dh (right) at a flux of 100 μg/cm^{2}h for 1000 h. Metal damage shown represent typical views across the samples' cross-sectioned planes. The images show that internal penetration is deeper for both Dw exposed samples (Fig. 7, right).

Fig. 8 compares the influence of grain boundaries on 347HFG steel corrosion for the deposit Dw and Dh at 500 h and at a deposit flux of 50 μg/cm^{2}h. These regions, according to Pettersson et al. [6], form K_2CrO_4. As such, the presence of K and Cr in the EDX maps gathered here were of interest. Although K-Cr interaction was not always indicated within the

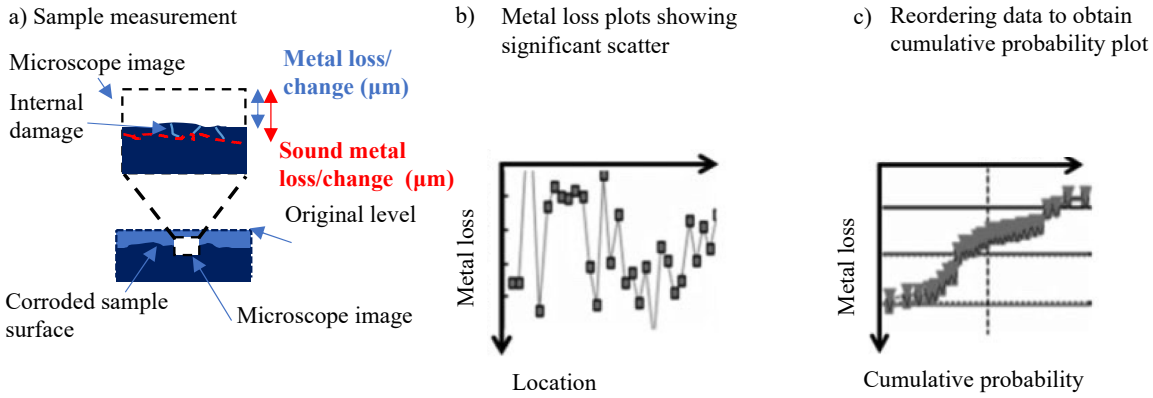


Fig. 3. Stages of dimensional metrology for determining metal loss: (a) sample is placed on calibrated optical microscope stage and micrographs are captured along post-exposure the metal surface, also capturing internal damage; (b) metal loss/change from comparing pre- and post-exposure dimensions, however, data is scattered; (c) data is reordered by damage severity, as such cumulative probability of damage is determined and can be quantitatively compared with other samples. . Adapted from [22]

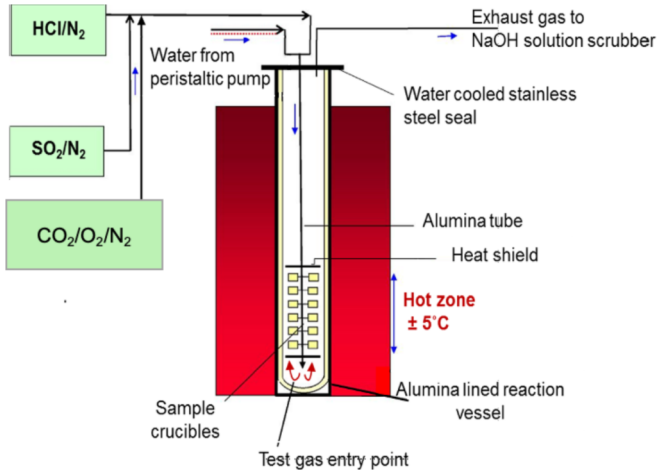


Fig. 4. Schematic of furnace setup for corrosion testing (BS ISO 17224:2015 [29]). .
Adapted from [20]

347HFG-Dh sample images, Fig. 7 and Fig. 8a show Na-K interactions for 347HFG-Dw. In addition, both 347HFG-Dw and 347HFG-Dh, show Cl (linked to many fireside corrosion mechanisms [6]) clustered at grain boundary locations where Ni is also observed, and the selective dissolution of Fe and Cr has occurred. The presence of Cl in the internal corrosion zone of 347HFG-Dh suggests K mobility is favoured in the Dh deposit system (KCl being the source of Cl in Dh). K, however, was not detected post-exposure (in 347 HFG-Dh), suggesting the prevailing fireside corrosion mechanism for Dh promotes the vaporisation of K.

For the Dw-347HFG sample (Fig. 8a), K and Na are deposited at a Fe and Cr depleted grain region. Also, Na is observed within grain boundaries, ~ 15 µm above the Cl cluster (at the internal corrosion zone). The absence of K at this grain boundary region suggests dissimilarities in corrosion mechanisms for the alkali metals within Dw in the exposure conditions.

Ca was sparingly detected at the metal/scale interface for samples tested with Dw at 600 °C. As scale delamination aids the removal of top-layer deposit residues, it is anticipated that $CaSO_4$ retained at the deposit layer would be shed from the sample (Fig. 8b). The preservation of Ca within the deposit region can be understood by reference to the $CaSO_4$-K_2SO_4 binary diagram described by Rowe et al. [32]. An intermediate crystalline phase, $K_2SO_4.2CaSO_4$ (calcium langbeinite), which melts at about 1000 °C, and a eutectic salt system which melts at 875 °C are said to exist. Thus at 600 °C, $CaSO_4$ is expected to remain in solid phase.

3.4. Mass transfer rates of KCP components

The KCPs vapour condensation rates have been calculated, by applying Eq. (1), to compare the corrosive components deposit fluxes for the HGB and WWF fuel categories. This calculation is simplistic and assumes a surface initially clean of deposits upon which vapour condensation is driven across a temperature gradient only. The vapour condensation flux '$m_{c,i}$' of a component, 'i' towards a heat exchanger surface have been estimated for each KCP. 'P_i' is the vapour pressure of the component at 1100 °C, 'P_{si}' is the saturated vapour pressure of the component at the heat exchanger surface (at 600 °C), 'P' is the overall gas pressure and 'ρ_g' is the flue gas density at 1100 °C. The vapour pressures have been calculated from their thermodynamically predicted gas phase concentrations at 1100 °C. A mass transfer coefficient of a condensing component, 'β_i', towards an area of the metal surface is a function of the metal tube diameter, 'd_t', Sherwood number, 'Sh', and the diffusion coefficient 'D_i' of the component.

$$M_{c,i} = \beta_i \left(\frac{P_i - P_{si}}{P} \right) \rho_g \quad (1)$$

$$\beta_i = ShD_i/d_t \quad (2)$$

[11,33,34].

Sh has been calculated using:

$$Sh = 2 + [0.552 * Re^{1/2} * Sc^{1/3}] \quad (3)$$

[11,33,34]

Reynold number, 'Re', and Schmidt value, 'Sc', have been calculated using:

$$Re = \frac{inertia\ forces}{viscous\ forces} = \rho_g \upsilon_g d_t / u_g \quad (4)$$

$$Sc = \frac{viscous\ diffusion\ rate}{mass\ diffusion\ rate} = u_g / \rho_g D_i \quad (5)$$

[11,33,34]Where 'ρ_g' is the flue gas density, 'υ_g' is the flue gas velocity and 'u_g' is the flue gas dynamic viscosity. The calculation parameters are listed in Table 7.

The partial pressure for each KCP component, 'P_i', is calculated at the flue gas stream at temperature 'T'= 1100 °C, using the ideal gas law relationship (Eq. (6)) where P_{total} = 1 atm. The saturation pressure, 'P_{si}', is in relation to condensation at the metal surface (600 °C, [11,34,38]), as expressed in Eq. (7).

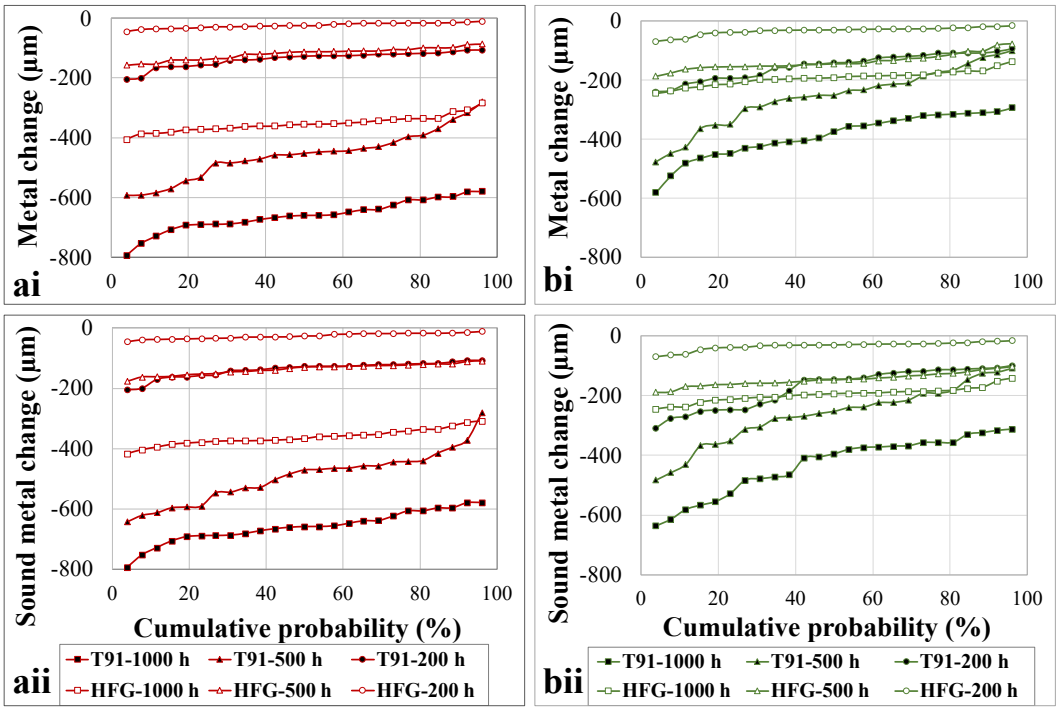


Fig. 5. Cumulative probability plots showing distributions of metal and sound metal changes (i & ii respectively) measured along the cross-sectioned T91 and 347 HFG sample planes. The further away the plot is from the x-axis, the greater the metal loss is. Samples have been exposed to deposits (a) Dw and (b) Dh in WWF test gas conditions at a deposit flux of 100 µg/cm^{2}h.

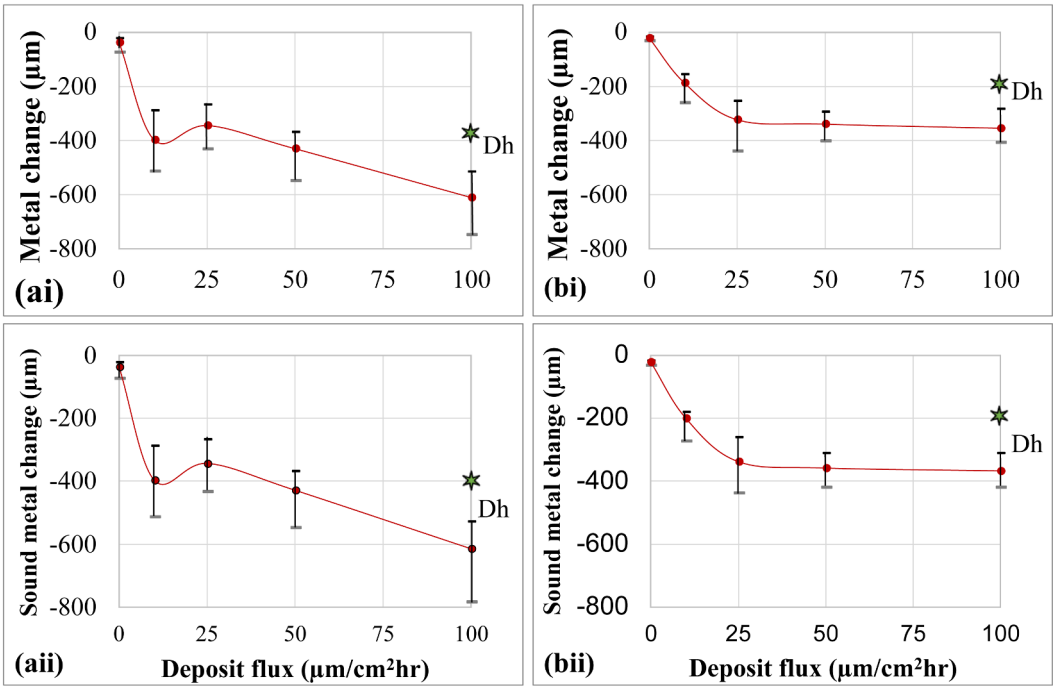


Fig. 6. Metal and sound metal changes (i & ii respectively) of cross-sectioned (a) T91 and (b) 347 HFG samples exposed to deposit D*w* at varying fluxes for 500 h Metal changes for the Dh deposit at a flux of 100 µg/cm^{2}h are also presented.

$$P_i/P_{total} = n_i/n_{total} \quad (6)$$

$$Psi = P_n \exp(A_i - \frac{B_i}{T - C_i}) \quad (7)$$

'*A*', '*B*' and '*C*' are given constants [11,34] used to calculate the saturation partial pressure of '*i*'. The KCP compounds partial pressures, '*Pi*', for both fuel categories calculated from thermodynamic combustion simulations at 1100 °C are listed in Table 8.

Applying Eqs. (1) to (7) and the partial pressure values in Table 8, the KCP vapour condensation fluxes on clean tube surfaces are listed in Table 9.

The calculated vapour condensation fluxes (Table 9) are based on

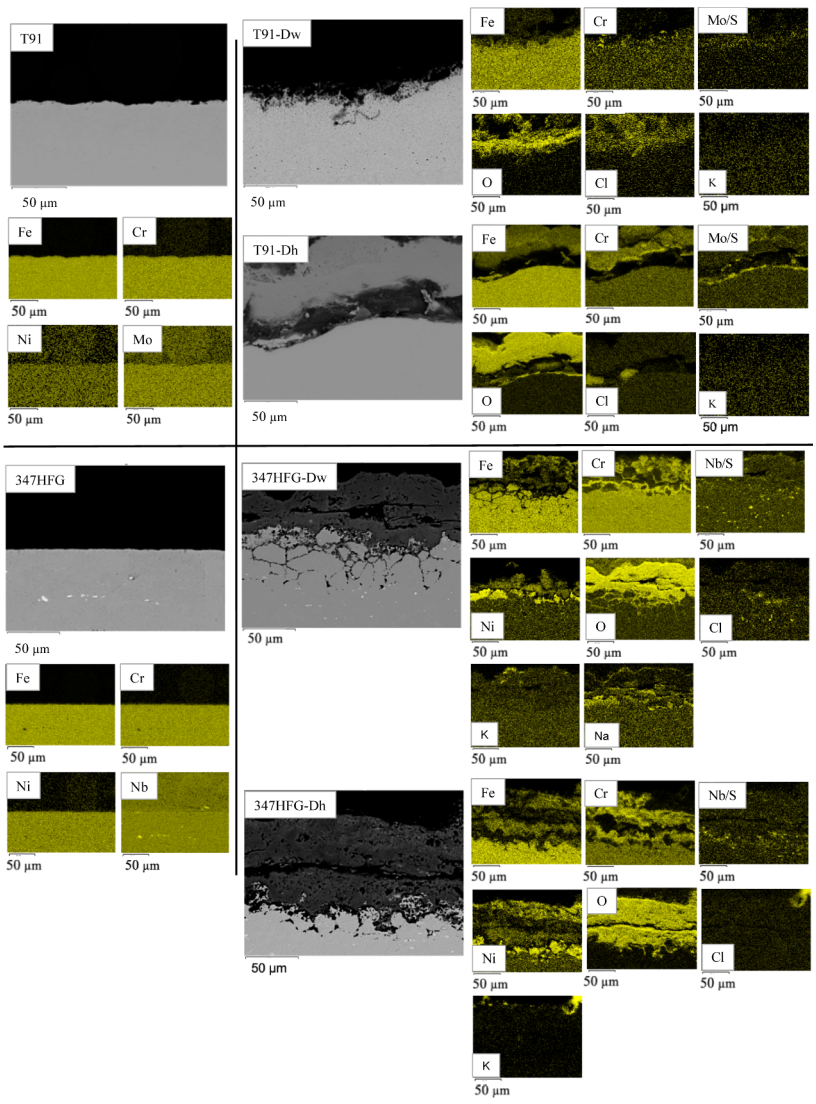


Fig. 7. BSE images (grey-scale) and EDX mappings (yellow-scale) of T91 (top) and 347HFG (bottom). Unexposed reference images of both alloys are on the left. EDX peak overlaps on 347HFG and T91 have been identified for Nb/S and Mo/S respectively. Samples with deposit following 1000 h exposure in WWF test gas conditions at 600 °C and a deposition flux of 100 µg/cm^{2}h are shown on the right. (For interpretation of the references to colour in this figure legend, the reader is referred to the web version of this article.)

equal fuel feed rates (kg/hour) into a combustor, whereas the energy contents and moisture levels of the fuels are different (Table 1). For plant operations, heating values are improved for dry feeds, however deposition fluxes on tube surfaces are expected to increase with drying, as the fuel feed becomes more concentrated, especially for HGB fuels which typically have higher 'as received' moisture levels than wood. Thus, the vapour condensation flux margin between both fuel categories is expected to be wider.

4. Discussion

4.1. Fireside corrosion influence of deposits Dw and Dh

MTData thermodynamic predictions suggest the KCP for WWF comprises of both alkali metals, K and Na, while deposit Dh for the HGB category comprises only of K cations. The deposit compositions represent molten components only, not considering the unreactive ash deposit fraction. Simms et al. [20] employed a deposit with 92.5 wt% fly ash diluting the KCP compounds, while investigating deposit corrosivity on alloy samples at 600 °C. The application flux of the potentially active species (i.e. the KCP), KCl and K_2SO_4, were 5 and 2.5 µg/cm^{2}h respectively. ~20 µm metal thickness change to 347HFG was recorded at 10% metal loss exceedance, following 1000 h exposure. In contrast, KCl and K_2SO_4 application fluxes (for example) carried out in this study were both 50 µg/cm^{2}h (for deposit Dh). ~480 µm metal thickness change at 10% exceedance (Fig. 5) was observed for the austenitic steel at 600 °C following 1000 h exposure. The higher metal damage rates encountered by samples evaluated in this study are thus owed to the increased exposure flux of KCP compounds. Omitting other potential but unreactive deposits from the compound mixture, for example in Table 3, simplifies the comparison of the KCP corrosion influences.

Metal loss is more severe for the Dw deposit exposed samples when deposit chemistries are compared at the same deposition flux. Cl transport to the internal corrosion zone region for sample 347HFG-Dw exposed for 1000 h also appears more pronounced (~40 µm penetration depth from metal surface) compared to that of 347HFG-Dh (~20 µm penetration depth from metal surface) (Fig. 7, right). The single cation (Dh) deposit system is limited to K cation reactions, whereas additional reaction combinations will occur in the Na-K deposit system (Dw). The greater damage depths observed for the Na-K exposed austenitic steel sample, 347HFG-Dw, than seen for the single cation exposed sample, 347HFG-Dh, (Fig. 7) correlates with findings by He et al. [39], who compared the corrosion damages between single and double cation salt systems at 700 °C. The most damaging of He et al.'s salt combinations were NaCl-KCl and Na_2SO_4-K_2SO_4 mixtures (50/50 wt%), the former being most penetrative. Meanwhile, their single cation deposit mixtures (KCl-K_2SO_4 and NaCl-Na_2SO_4; 50/50 wt%) showed the least severe damages. The authors, however, did not expound on reasons for the

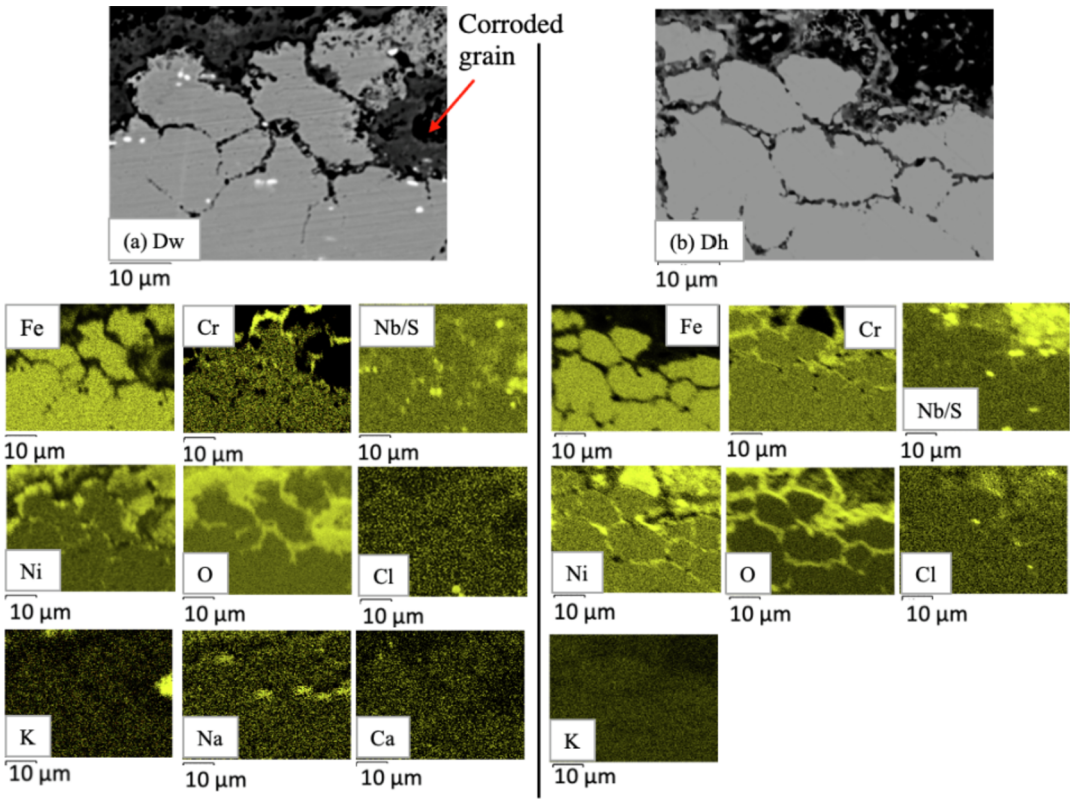


Fig. 8. Grain boundary damages on 347HFG samples exposed to (a) Dw and (b) Dh at flux 50 µg/cm^{2}h for 500 h in WWF test gas conditions at 600 °C.

Table 7
Vapour condensation parameters used in Equation (1)-Equation (5).

Parameter	Input value
Flue gas density, ρ_g (kgm^{-3}) [35]	0.2571
Tube diameter, d_t (m) [11]	0.038
Flue gas dynamic viscosity at 1100 °C, u_g (Pa.S) [35]	5.01×10^{-5}
Flue gas velocity, v_g (ms^{-1}) [36]	5.80
Diffusion coefficient, $D_{i_{(KCl)}}$ (m^{2}s) [36]	1.36×10^{-4}
Diffusion coefficient, $D_{i_{(K_2SO_4)}}$ (m^{2}s) [36]	9.06×10^{-5}
Diffusion coefficient, $D_{i_{(Na_2SO_4)}}$ (m^{2}s) [37]	1.08×10^{-5}

Table 8
Partial pressure values quantified from simulated flue gas compositions occurring at 1100 °C. $CaSO_4$ is assumed to be deposited as particulate for heat exchange deposition rate calculations.

KCP compounds	Partial pressure, 'P_i' (Pa)	
	WWF	HGB
KCl	4.68	21.36
K_2SO_4	0.22	2.29
Na_2SO_4	0.16	–

Table 9
Calculated KCP mass transfer fluxes, '$M_{c,i}$', at heat exchanger surface temperatures of 600 °C.

KCP compounds	WWF		HGB	
	'M_{ci}' (µg/cm^{2}h)	% Molar ratios	'M_{ci}' (µg/cm^{2}h)	% Molar ratios
KCl	295	97.9	1566	96.6
K_2SO_4	12	1.7	129	3.4
Na_2SO_4	2.14	0.4	–	–

corrosion difference between mixed and single cation deposits. Also, damage due to mixed cation/mixed anion deposit systems (for example, KCl-Na_2SO_4) were not directly compared.

The increased scale spallation observed on T91 with increasing deposit flux can be attributed to the severe Cl attack, confirmed in Fig. 7, and possible sulphation [40]. However, it can be certain that corrosion depths in the austenitic steel samples were not proportional to chloride flux (Table 4), otherwise internal penetration for the Dh exposed samples would be greater.

Having observed that the 30/70 mol.% chloride/sulphate deposit system (Dw) could cause greater damage than the 70/30 mol.% chloride/sulphate deposit system (Dh) (Fig. 5), it becomes necessary to consider the cations' role.

$$2((Na,K)Cl) + 1/2O_2 + H_2O + 2e^- \rightleftarrows 2((Na,K)OH) + 2Cl^- \quad (8)$$

Cl attack, described by ion diffusion [41] (Eq. (8)), utilises alkali metal components. To evaluate the high temperature corrosivity of salts, Karlsson et al. [13] used EDX to observe K_2CrO_4 and Na_2CrO_4 scale formation from protective oxides on 304L steel exposed to KCl and NaCl (respectively) in a 40 % H_2O, 5% O_2 (N_2 bal.) atmosphere at 600 °C (Eq. (9)).

$$8(Na,K)Cl + 2Cr_2O_{3_{(s)}} + 3O_2 + 4H_2O \rightleftarrows 4\left((Na,K)_2CrO_4\right)_{(s)} + 8HCl_{(g)} \quad (9)$$

A current (Eq. (10)), driven by oxidation [41], provides electrons which facilitate the electrochemical decomposition process of the alkali metal scales formed in Eq. (9).

$$Cr_{(s)} \rightleftarrows Cr^{3+} + 3e^- \quad (10)$$

As such, the electrochemically assisted decomposition of alkali metal chromate or ferrite releases alkali metal-OH at the scale surface (Eq. (11)) which would either react further with oxide scales or be volatilized.

$$(Na,K)_2CrO_{4_{(s)}} + H_2O_{(g)} + 3e^- \rightleftarrows 2((Na,K)OH)_{(l,g)} + Cr_2O_{3(s)} \quad (11)$$

Karlsson et al. [13] however, observed difference between the K_2CrO_4 and the Na_2CrO_4 decomposition rates. The rate disparity was explained by the higher volatility of KOH compared to NaOH (equilibrium vapour pressure at 600 °C: $4.9X10^{-5}$ and $5.3X10^{-7}$ bar for KOH and NaOH respectively [13]). Thus, NaOH formed by the decomposition of Na_2CrO_4 (Eq. (11)) accumulated, while KOH easily evaporated.

In conclusion, alkali metal ions are damaging to Fe oxide scales at 600 °C (Eq. (9)), however, the loss of K^+ ions as KOH may limit the damage influence of these species to such scales. At combustion gas water vapour levels as low as 1 ppm, Eqs. (8) and (9) can proceed under WWF (~10 mol.% H_2O) exposure conditions at 600 °C [42].

The following can be deduced:

i. Where Cl^- ion diffusion is reliant on K availability (Eq. (8)), the damage rate of Fe oxide (Eq. (9)) may not be sustained as KOH is lost from the system. Eq. (11) explains the lack of K in 347HFG-Dh post-exposure (Fig. 8b).
ii. Cl^- ion diffusion dependent on both Na^+ and K^+ ions (in the case of deposit Dw), will be more sustained due to increased alkali metal ion retention (as NaOH). The positioning of Na, relative to the Cl cluster at the internal corrosion zone (Fig. 8a) suggests a prevalent role of Na^+ ions in the penetrative Cl^- ions attack for 347HFG-Dw.
iii. In addition, the presence of similarly positioned K and Na species within a Fe-Cr depleted and corroded grain in sample 347HFG-Dw (Fig. 8a), suggests similarities in the alkali metal reaction mechanisms, and may indicate the presence of a Na-K eutectic.

To summarise, while both deposit systems result in severe damage, surface and internal damage is more extensive in the Na-K system where the chloride ion level (30 mol.%) is sufficient for Cl^- ion assisted damage. The increased corrosion damage of Dw, relative to Dh, can also be related to the lower eutectic melt temperatures attainable in the Na-K system, compared to the K-cation system [31], which is in line with the lower temperature range of KCP concentration profiles for WWF presented in Fig. 1. Evaluation of the KCP chloride and Na concentration thresholds required to maintain the higher corrosivity of a Na-K deposit (than a K deposit system) would enable further categorisation of WWF fireside corrosion behaviour.

4.2. Deposit compositions

There are numerous routes to the deposition of material on a heat exchanger surface (such as stickiness probabilities, deposit shedding, direct impaction) [34], however this research focusses on vapour condensation, omitting these other deposition/deposit loss routes. The mass transfer values calculated (Table 9) enabled the comparison of the alkali deposition fluxes for the fuel categories based on parameters listed in Table 7.

The deposition fluxes calculated for heat exchangers are increased for HGB combustion compared to WWF (Table 9) which is the reason for the enhanced fireside corrosion rates of heat exchangers encountered during HGB fuel firing [3]. There are, however, disparities between the deposit compositions predicted by MTData (Table 4) and those determined from mass transfer rate calculations (Table 9).

While a combustion gas stream is cooling, the constituent components could be expected to undergo changes, which MTData can be used to approximate, assuming thermodynamic equilibrium. Some of these gas composition changes are illustrated in Fig. 9. Due to the changes in stable compounds with temperature, the condensing gas species and condensate compositions calculations are different. One example of these thermodynamically-predicted changes are the important gas phase reactions (relating to fireside corrosion) illustrated in Eqs. (12) and (13), where the sulphation of alkali metal chlorides leads to alkali deposition as sulphates [33].

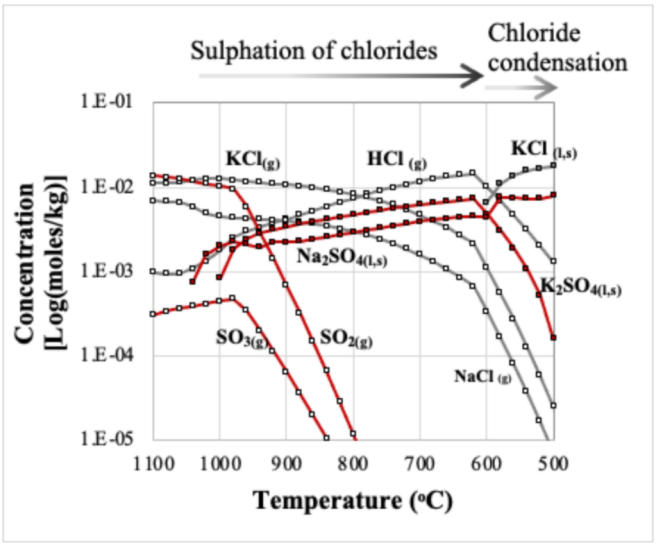


Fig. 9. MTData predicted alkali metal association changes occurring across the condensation temperature range. Composition outputs have been simulated for WWF (median values) combustion at 8:1 air/fuel feed ratio (kg/kg). (g) denotes gas phase, (l,s) denotes liquid/solid (or condensed) phases.

$$4(((Na,K)Cl)_{(g)} + 2SO_{2_{(g)}} + O_{2_{(g)}} + 2H_2O_{(g)} \rightarrow 2\left((Na,K)_2SO_4\right)_{(l,s)} + 4HCl_{(g)} \quad (12)$$

$$4((Na,K)Cl)_{(g)} + 2SO_{3_{(g)}} + 2H_2O_{(g)} \rightarrow 2\left((Na,K)_2SO_4\right)_{(l,s)} + 4HCl_{(g)} \quad (13)$$

The Cl/sulphate alkali metal transitions predicted by MTData (Fig. 9) show two distinct condensation behaviours for WWF firing:

i. At 1050–600 °C, the alkali metal sulphate condensation flux increases (similar behaviour is noted by [43]). Thermodynamic simulation shows no Cl-containing phase condensation occurs (defined as present at levels above 10^{-5} mol/kg fuel) within this temperature range. This temperature range is also characterised by an increase in HCl gas concentration and subsequent drop in gas phase alkali metal and sulphate content. These compositional change trends align with Eqs. (12) and (13).
ii. Below 600 °C, the condensation of $KCl_{(g)}$ as $KCl_{(l,s)}$ becomes dominant. It is likely that the corresponding drop in $K_2SO_{4(l,s)}$ and $HCl_{(g)}$ is related to the proposed reaction given in Eq. (14):

$$K_2SO_{4_{(s)}} + 2HCl_{(g)} \rightarrow 2KCl_{(g)} + SO_{3_{(g)}} + H_2O_{(g)} \quad (14)$$

At 620 °C (Fig. 9), $NaCl_{(g)}$ is sulphated by SO_3 (released in Eq. (14)), contributing to the rapid increase in Na_2SO_4 condensate, according to Eq. (13).

By contrast, the KCP (and fluxes) obtained from the mass transfer rate prediction model (Table 9) assume alkali metal associations will be maintained during condensation, despite the temperature gradient from bulk gas to alloys surface. As this technique assumes no chemical changes, it may be unsuitable for predicting alkali metal deposition from biomass firing.

These discrepancies in the final composition of the condensed deposit, obtained from these two methodologies, highlight a major challenge in fireside corrosion evaluation. Similarly, data (e.g. swabs) taken in maintenance periods from plants are known to have potentially different chemistries than would be anticipated under operating conditions. The alkali metal sulphate/chloride ratio of cooled deposits will be different at firing conditions [44]. MTData thermodynamic condensed phase KCP compositions (Table 4) more closely resemble Cl/sulphate ratios of several deposit samples collected by Michelson et al.

[7] on air-cooled probes in a 10 MW straw fired boiler.

5. Conclusion

The corrosive properties of key condensed phase (KCP; compounds of corrosive tendencies at heat exchanger temperature range, 450-600℃) deposits occurring in WWF and HGB fuels have been evaluated at 600 °C on sectioned 347HFG and T91 tube samples. The deposits and gas compositions used were derived from thermodynamic simulations, by MTData, at 600 °C and 1100 °C respectively. While the vapour condensation demonstrated the much higher deposit fluxes occurring for HGB fuels compared to WWF (~5 times higher for HGB), the MTData deposit compositions (with K/Na/Ca sulphates and chlorides for WWF and KCl/K_2SO_4 for HGB), were more realistic, as determined by comparison with the Cl/sulphate ratios of power plant deposits in literature.

The fireside corrosion rates encountered in this study did not correlate with deposits' Cl contents. Indeed, the multi-cation WWF deposit Dw, with 30/70 mol.% Cl/sulphate (30 mol.% KCl, 20 mol.% K_2SO_4, 20 mol.% Na_2SO_4, 30 mol.% $CaSO_4$), caused more corrosion attack on both steels at a deposit application flux of 100 μg/cm^2h than the single-cation HGB deposit Dh, with 70/30 mol.% Cl/sulphate (70 mol.% KCl, 30 mol.% K_2SO_4). The corrosion damage differences between both deposits were related to:

i. The lower vapour pressure of decomposing scale products, NaOH compared to KOH. Compared to KOH, NaOH may be retained more at corrosion sites (slower evaporation rate), thus promoting further alkali metal assisted corrosion attack.
ii. The lower eutectic melting temperatures attainable in a combined alkali metal system. Thermodynamic data demonstrated different peak molten temperature ranges for the deposit components which is lower for Dw (500–600 °C) than Dh (580–720 °C).

The nature of fireside corrosion damage influenced by WWF combustion has thus been more clearly defined as being less deleterious than corrosion damage due to HGB firing on the basis of the lower heat exchanger deposit fluxes encountered when WWF are employed in biomass firing. This work has however found the WWF deposit to be more damaging than HGB deposit at the same KCP deposition flux.

Declaration of Competing Interest

The authors declare that they have no known competing financial interests or personal relationships that could have appeared to influence the work reported in this paper.

Funding

The author(s) are grateful for the financial support provided by BF2RA towards this research, and also to Cranfield University for Industrial Partnership PhD scholarship support.

References

[1] Aldridge J. UK Wood Pellet Imports Hit Record April High. Available at: Argus Media 2020;26. https://www.argusmedia.com/en/news/2118063-uk-wood-pellet-imports-hit-record-april-high.
[2] Wood Recyclers Association. UK Could Start to Import Waste Wood Biomass. WRA. September 2019; Available at: https://woodrecyclers.org/uk-could-start-to-import-waste-wood-biomass/(Accessed: 1 March 2021).
[3] Wiltsee G. Lessons Learned from Existing Biomass Power Plant. California: National Renewable Energy. Laboratory 2000. Available at: 10.2172/753767.
[4] Vassilev S V., Baxter D., Vassileva CG. An overview of the behaviour of biomass during combustion: Part II. Ash fusion and ash formation mechanisms of biomass types. Fuel. 2014; 117(PART A): 152–183. Available at: 10.1016/j.fuel.2013.09.024.
[5] Okoro SC., Kiamehr S., Montgomery M., Frandsen FJ., Pantleon K. Effect of Flue Gas Composition on Deposit Induced High Temperature Corrosion Under Laboratory Conditions Mimicking Biomass Firing. Part I: Exposures in Oxidizing and Chlorinating Atmospheres. Materials and Corrosion. 2017; Available at: 10.1002/maco.201609173.
[6] Pettersson J., Folkeson N., Johansson L-G., Svensson J-E. The Effects of KCl, K2SO4 and K2CO3 on the High Temperature Corrosion of a 304-Type Austenitic Stainless Steel. Oxidation of Metals. 2011; 76(1–2): 93–109. Available at: 10.1007/s11085-011-9240-z.
[7] Michelsen HP., Frandsen F., Dam-Johansen K., Larsen OH. Deposition and High Temperature Corrosion in a 10 MW Straw Fired Boiler. Fuel Processing Technology. 1998; 54(1–3): 95–108. Available at: 10.1016/S0378-3820(97)00062-3.
[8] Wilén C, Moilanen A, Kurkela E. Biomass Feedstock Analyses. Espoo: VTT Publications; 1996.
[9] Edo M., Björn E., Persson PE., Jansson S. Assessment of Chemical and Material Contamination in Waste Wood fuels – A case study ranging over nine years. Waste Management. Elsevier Ltd; 2016; 49: 311–31Available at: https://doi.org/10.1016/j.wasman.2015.11.048.
[10] Jermer J., Ekvall A., Tullin C. Analysis of Contaminants in Waste Wood. Stockholm; 2001. Available at: https://www.researchgate.net/publication/242161546_Analysis_of_contaminants_in_waste_wood (Accessed: 24 April 2019).
[11] Simms NJ. Environmental Degradation of Boiler Components. In: Oakey JE (ed.) Power Plant Life Management and Performance Improvement. Woodhead Publishing; 20pp. 145–179. Available at: 10.1533/9780857093806.2.145.
[12] Nielsen HP., Frandsen FJ., Dam-Johansen K., Baxter LL. Implications of Chlorine-Associated Corrosion on the Operation of Biomass-Fired Boilers. Progress in Energy and Combustion Science. 2000; 26(3): 283–298. Available at: 10.1016/S0360-1285(00)00003-4.
[13] Karlsson S., Pettersson J., Johansson LG., Svensson JE. Alkali Induced High Temperature Corrosion of Stainless Steel: The Influence of NaCl, KCl and CaCl2. Oxidation of Metals. 2012; 78(1–2): 83–102. Available at: 10.1007/s11085-012-9293-7.
[14] Sommersacher P, Brunner T, Obernberger I. Fuel Indexes : A Novel Method for the Evaluation of Relevant Combustion Properties of New Biomass Fuels. Energy Fuels 2011;26(1):380–90.
[15] Strandberg A., Skoglund N., Thyrel M., Lestander TA., Broström M., Backman R. Time-Resolved Study of Silicate Slag Formation during Combustion of Wheat Straw Pellets. Energy and Fuels. 2019; 33(3): 2308–2318. Available at: 10.1021/acs.energyfuels.8b04294.
[16] Meng X., Zhou W., Rokni E., Chen G., Sun R., Levendis YA. Release of Alkalis and Chlorine from Combustion of Waste Pinewood in a Fixed Bed. Energy and Fuels. 2019; 33(2): 1256–1266. Available at: 10.1021/acs.energyfuels.8b03970.
[17] Meadowcroft DB. A Code of Practice for Discontinuous Corrosion Testing in High Temperature Gaseous Atmosphere. Material Science Forum. 1997; 251(254): 973–978. Available at: https://doi.org/10.4028/www.scientific.net/MSF.251-254.973.
[18] Hussain T., Syed AU., Simms NJ. Fireside Corrosion of Superheater Materials in Coal/Biomass Co-Fired Advanced Power Plants. Oxidation of Metals. 2013; 80(5–6): 529–540. Available at: 10.1007/s11085-013-9394-y.
[19] in Guidelines for Methods of Testing and Research in High Temperature Corrosion: Working Party Report 1995:85.
[20] Simms NJ, Kilgallon PJ, Oakey JE. Degradation of Heat Exchanger Materials Under Biomass Co-Firing Conditions. Mater High Temp 2007;24(4):333–42. Available at: 10.3184/096034007X281640.
[21] Dudziak T., Hussain T., Orlicka D., Pokrywa A., Simms NJ. Fireside Corrosion Degradation of 15Mo3, T22, T23 & T91 in Simulated Coal-Biomass Co-Fired Environment. Materials and Corrosion. 2015; 66(9): 839–850. Available at: 10.1002/maco.201407886.
[22] Sumner J., Potter A., Simms NJ., Oakey JE. Hot Corrosion Resistance of Gas Turbine Materials in Combusted Syngas Environments. Materials at High Temperatures. 2015; 32(1–2): 177–187. Available at: 10.1179/0960340914Z.00000000098.
[23] ECN Phyllis 2. Database for Biomass and Waste. Available at: https://www.ecn.nl/phyllis2/(Accessed: 15 March 2018).
[24] MT Data. MT Data. 2011. Available at: https://www.phase-trans.msm.cam.ac.uk/mtdata/introduction.html (Accessed: 31 August 2018).
[25] Chang YN., Wei FI. High-Temperature Chlorine Corrosion of Metals and Alloys – A review. Journal of Materials Science. 1991; 26(14): 3693–3698. Available at: 10.1007/BF01184958.
[26] Global Steel & Alloys. ASTM A213/ASME SA213 T2, T11, T12, T22, T91, T92 Chemical Composition and Mechanical Properties. Available at: http://www.globalsteelalloys.com/astm-a213-t2-t11-t22-t91-t92-pipes-tubes-supplier-exporter.html (Accessed: 26 June 2019).
[27] Syed AU, Hussain T, Simms NJ, Oakey JE. Microscopy of fireside corrosion on superheater materials for oxy-fired pulverised fuel power plants. Mater High Temp 2012;29(3):219–28. Available at: 10.3184/096034012X13323635669332.
[28] BSI. ISO 26146:2012 Corrosion of Metals and Alloys — Method for Metallographic Examination of Samples After Exposure to High-Temperature Corrosive Environments. 2012.
[29] BSI. BSI Standards Publication Corrosion of metals and alloys — Test Method for High Temperature Corrosion Testing of Metallic Materials by Application of a Deposit of Salt , Ash , or other Substances. 2015. Available at: http://www.iso.org/iso/home/store/catalogue_tc/catalogue_detail.htm?csnumber=59473.
[30] FactSage. FACT Salt Databases: Database Documentation. 2019. Available at: https://www.crct.polymtl.ca/fact/documentation/(Accessed: 18 March 2019).
[31] Niu Y., Zhu Y., Tan H., Hui S., Jones JM., Yuanyi L. A Calculation Method of Biomass Slagging Rate Based on Crystallization Theory. Asia-Pacific Journal of Chemical Engineering. 2014; (9): 456–463. Available at: 10.1002/apj.

[32] Rowe JJ, Morey GW, Hansen ID. The Binary System K2SO4CaSO4. J Inorg Nucl Chem 1965;27(1):53–8.
[33] Riccio C. Improved Deposition Modelling for Heat Exchangers in Pulverised Fuel Combustors. Cranfield University; 2019.
[34] Tomeczek J., Palugniok H., Ochman J ózef. Modelling of Deposits Formation on Heating Tubes in Pulverized Coal Boilers. Fuel. 2004; 83(2): 213–221. Available at: 10.1016/S0016-2361(03)00219-9.
[35] Engineering Tool Box. Air – Density, Specific Weight and Thermal Expansion Coefficient at Varying Temperature and Constant Pressures. 2003. Available at: https://www.engineeringtoolbox.com/air-density-specific-weight-d_600.html (Accessed: 11 November 2020).
[36] Zhou H., Jensen PA., Frandsen FJ. Dynamic Mechanistic Model of Superheater Deposit Growth and Shedding in a Biomass Fired Grate Boiler. Fuel. 2007; 86 (10–11): 1519–1533. Available at: 10.1016/j.fuel.2006.10.026.
[37] Applin KR, Lasaga AC. The Determination of SO42-, NaSO4-, and MgSO40 Tracer Diffusion Coefficients and their Application to Diagenetic Flux Calculations. Geochim Cosmochim Acta 1984;48(10):2151–62.
[38] Thomson GW. The Antoine Equation for Vapor-Pressure Data. Chemical Reviews. 1946; 38(1): 1–39. Available at: 10.1021/cr60119a001.
[39] He J., Xiong W., Zhang W., Li W., Long K. Study on the High-Temperature Corrosion Behavior of Superheater Steels of Biomass-Fired Boiler in Molten Alkali Salts ' Mixtures. Advances in Mechanical Engineering. 2016; 8(11): 1–9. Available at: 10.1177/1687814016678163.
[40] Lu J., Huang J., Yang Z., Zhou Y., Dang Y., Yuan Y., et al. Simulated Fireside Corrosion Behavior of a Wrought Ni-Fe-Based Superalloy for 700 °C-Class Ultra-supercritical Power Plant Applications. Journal of Materials Engineering and Performance. Springer US; 2019; 28(12): 7390–7397. Available at: 10.1007/s11665-019-04515-z.
[41] Folkeson N., Jonsson T., Halvarsson M., Johansson LG., Svensson JE. The Influence of Small Amounts of KCl(s) on the High Temperature Corrosion of a Fe-2.25Cr-1Mo Steel at 400 and 500°C. Materials and Corrosion. 2011; 62(7): 606–615. Available at: 10.1002/maco.201005942.
[42] Lehmusto J., Yrjas P., Skrifvars BJ., Hupa M. High temperature corrosion of superheater steels by KCl and K 2CO 3 under dry and wet conditions. Fuel Processing Technology. Elsevier B.V.; 2012; 104: 253–264. Available at: 10.1016/j.fuproc.2012.05.020.
[43] Paneru M., Babat S., Maier J., Scheffknecht G. Role of Potassium in Deposit Formation During Wood Pellets Combustion. Fuel Processing Technology. Elsevier; 1 January 2016; 141: 266–275. Available at: 10.1016/j.fuproc.2015.10.008 (Accessed: 12 July 2018).
[44] Blomberg T., Tripathi T., Karppinen M. New Chemical Mechanism Explaining the Breakdown of Protective Oxides on High Temperature Steels in Biomass Combustion and Gasification Plants. RSC Advances. Royal Society of Chemistry; 2019; 9(18): 10034–10048. Available at: 10.1039/c9ra00582j.



https://dspace.org/

A comparative evaluation of waste wood and herbaceous biomass fireside corrosion behaviours

Sanusi, Toyin; Sumner, Joy; Simms, Nigel J.

2022-05-13
Elsevier
https://doi.org/10.1016/j.fuel.2022.124070
Sanusi T, Sumner J, Simms NJ. (2022) A comparative evaluation of waste wood and herbaceous biomass fireside corrosion behaviours. Fuel, Volume 324, Part A, September 2022, Article number 124070

Downloaded from a DSpace repository. https://dspace.org/